Chemical Physics Impact 6 (2023) 100191

Contents lists available at ScienceDirect

Chemical Physics Impact

journal homepage: www.sciencedirect.com/journal/chemical-physics-impact

$Cu_xMn_{1-x}Fe_2O_4$ as oxygen carrier for chemical looping steam methane reforming

Mousa Nazari [a], Nahid Ghasemi [b,*], Mohammad Mansoob Khan [c,*], Mahsaalsadat Rokni [d], Seyed Reza Taghavi [a]

[a] Department of Chemical Engineering, Imam Hossein Comprehensive University, Tehran, Iran
[b] Department of Chemical and Biochemical Engineering, The University of Western Ontario, London, Canada
[c] Chemical Sciences, Faculty of Science, Universiti Brunei Darussalam, Jalan Tungku Link, Gadong, BE 1410, Brunei Darussalam
[d] Iran Avandfar Company, Department of Quality Control, Karaj, Iran

ARTICLE INFO

Keywords:
$Cu_xMn_{1-x}Fe_2O_4$ oxygen carrier
Spinel-ferrites structure, CL-SMR process
RSM, H_2 production

ABSTRACT

The spinel-ferrite structure (SFS) oxygen carrier (OC) $Cu_xMn_{1-x}Fe_2O_4$ with (x = 0.3, 0.5, 0.6, and 0.7) was synthesized by the co-precipitation technique to be used in the chemical looping steam methane reforming process (CL-SMRP). The SFS OCs were characterized using Fourier Transform infrared spectroscopy (FT-IR), powder X-ray diffraction (XRD), Field emission scanning electron microscopy (FE-SEM), Energy-dispersive X-ray spectroscopy (EDX), Thermogravimetric Analysis (TGA), and Brunauer-Emmett-Teller (BET). The Response Surface Methodology (RSM) based on the Box-Behnken model was employed to estimate the effects of independent variables and their interactions on the OC activity. The effects of temperature, OC, loading percentage, steam to methane molar ratio, the number of redox cycles on the H_2 production yield (Y_{H_2}), methane conversion(X_{CH_4}), and $S_{CO/CO2}$ were determined. According to the analysis of variance (ANOVA) analysis, results indicated that the reaction temperature and the OC (x) have extremely significant effects on X_{CH_4} and Y_{H_2}. The maximum X_{CH_4} of 98.7%, Y_{H_2} of 81.02%, and $S_{CO/CO2}$ of 6.54 were obtained at optimal value conditions such as 650 °C, SFS OC $Cu_{0.6}Mn_{0.4}Fe_2O_4$, S/C 2.5, and redox cycle 30.

1. Introduction

Pollution from fossil fuels is one of the most significant problems that are faced by human society in recent years. Fossil fuels, especially natural gasses, are one of the most essential sources that are widely used as energy sources in various industries. The main problems of these fuels are the production of greenhouse gasses, CO, CO_2, SO_x, etc. [1].

Therefore, the need for alternative fuels for this type of fuel is increasing day by day. Hence, alternative energy carriers such as hydrogen (H_2) gas, have been investigated [2]. H_2 is considered a suitable alternative as a clean and renewable fuel because during its combustion process, it does not emit greenhouse gasses and acid. It only produces water vapor. Fossil fuels such as natural gas and coal has been used as raw materials for H_2 production. Today, a large amount of the H_2 required by the industry is produced from hydrocarbon fuels, including natural gasses[1–4]. H_2 production using the steam methane reforming process (SMRP) is one of the most common and economical H_2 production methods. But capturing and storing CO_2 is difficult and complex. Here, chemical looping (CL) processes for H_2 production have been considered because of the high purity of H_2 without the use of air or H_2 separation units and CO_2 uptake. CL process is a suitable method for producing H_2 and synthesis gas from SMR process. In these processes, the lattice oxygen (LO) of oxygen carrier (OC) structure is used instead of pure oxygen in CH_4 oxidation reaction [5–10]:

$$\text{Reduction: } Me_xO_y + \delta CH_4 \rightarrow Me_xO_{y-\delta} + \delta(CO + 2H_2) \quad \text{(i)}$$

$$\text{Oxidation: } Me_xO_{y-\delta} + \delta H_2O \rightarrow Me_xO_y + \delta H_2 \quad \text{(ii)}$$

$$\text{Overall reaction: } CH_4 + H_2O \rightarrow 3H_2 + CO \quad \text{(iii)}$$

where "M", "Me_xO_y", and "$Me_xO_{y-\delta}$ " represent the metal, SFS OC, and correspond to the reduced spinel ferrite (SF) OC, respectively. The CL-SMR reaction can be interpreted as SMR, as seen in the overall reaction (iii). The most significant effective parameter for the CL-SMR process is the selection of suitable OC, which should have very high X_{CH_4}, high H_2 selectivity, resistance to accumulation and temperature,

* Corresponding authors.
E-mail addresses: anahid3@gmail.com (N. Ghasemi), mmansoobkhan@yahoo.com (M.M. Khan).

https://doi.org/10.1016/j.chphi.2023.100191
Received 19 December 2022; Received in revised form 22 February 2023; Accepted 3 March 2023
Available online 5 March 2023

negligible carbon deposition, nontoxic, and environmentally friendly [8–10]. Various metals such as Co, Mg, Fe, Ni, Cu, and Mn have been considered as OCs for CL process [11–16]. Among them, Fe-based OCs were established to be very active in the CL-SMR for H_2 production [17, 18]. The Fe oxide reduction includes three phases: (a) $Fe_2O_3 \rightarrow Fe_3O_4$, (b) $Fe_3O_4 \rightarrow FeO$, and (c) $FeO \rightarrow Fe$.

The reduction of Fe_2O_3 to Fe_3O_4 is swift, where H_2 and CO are converted to H_2O and CO_2, respectively. The other stages have slow rates and low feed conversions. Due to the thermodynamic equilibrium, the second step ($Fe_3O_4 \rightarrow FeO$) is suitable for the CL-SMR process [19–21]. Iron oxides can lead to higher CO_2 reduction capacity compared to other metal oxides (MOs), but iron oxide was rapidly deactivated due to the agglomeration of particles on the OC surface. To prevent this phenomenon, different MOs can be combined with iron oxides. The combined MOs may be an appropriate candidate for OC, due to good reactivity and selectivity [18]. Incorporating support materials to the Fe-based OC in the CL and CL-SMR processes prevent their sintering and decrease the oxygen transport capacity [19,21,22]. The SFS with the general A-Fe_2O_4, where A = Ni, Cu, Co, Mn, and Zn have an appropriate catalyst performance [13,23–26]. To produce H_2 and CO_2 through the H_2 chemical looping (CLH) process, the SFS $NiFe_2O_4$, and $CoFe_2O_4$ are investigated as OCs [25], where it has shown that, under the same redox conditions, the SFS OCs have a higher capability in H_2 production compared to Fe_2O_3. The total amount of H_2 produced by SFS $NiFe_2O_4$ and $CoFe_2O_4$ OCs is four times more than Fe_2O_3 OC. Moreover, the SF had about 100% X_{CH_4} efficiency, while Fe_2O_3 had 22% X_{CH4} efficiency. The performance of SFS $NiFe_2O_4$ OC was investigated in the CL dry reforming of methane. The results indicated that Fe (metallic) could be oxidized to Fe_3O_4 through CO_2, while Ni (metals) cannot [26]. The oxidation capacity of NiO > synthetic SFS $NiFe_2O_4$ > mixed MOs NiO-Fe_2O_3 > Fe_2O_3, while the reduction capacity of synthetic SFS $NiFe_2O_4$ > mixed MOs NiO-Fe_2O_3 > Fe_2O_3 > NiO. The redox capability of synthesized SFS $NiFe_2O_4$ was much better than that of the NiO-Fe_2O_3 metal mixed MOs [26]. The SFS A-Fe_2O_4 as OCs in the CLC were studied. The SFS Ni, Cu, and Co are more capable of transferring LO than SFS Mn. The SFS Cu was very active, with 95% X_{CH_4}, while SFS Mn had the lowest activity of 30%. The X_{CH_4} for SFS Co, Ni, and Zn were 78, 90, and 68%, respectively [19]. The oxygen-free SFS can provide the LO through CO_2 oxidation and lead to CO_2 reduction to a significant extent, the SFS Ni OC in H_2 production can perpetrate a suitable reaction in several successive redox cycles in the CL process [18].

SFS are able to transfer their lattice oxygen to the fuel in the reduction stage and then obtain their lattice oxygen to some extent in the oxidation stage in the presence of air. Cu ferrite is very active and has a very high CH_4 conversion percentage, and compared to Mn ferrite, it has a greater ability to transfer lattice oxygen. The CH_4 conversion percentage of Mn ferrite is very low. In addition, its oxygen transfer capacity is very low and its lattice oxygen is not easily released. Therefore, the reaction faces a lack of oxygen, which causes partial oxidation of CH_4 and is an advantage for H_2 production. On the other hand, Cu easily releases its lattice oxygen, which increases its selectivity towards CO_2. Therefore, the increase of Cu to the OC causes selectivity towards CH_4 and CO_2, and the addition of Mn causes the reaction to lack oxygen, as a result, the production of CO_2 decreases [8,27,28]. The mixture of several MOs can lead to an increase in OC efficiency. The SFS, with various composition has suitable performance. The mixture of different metals improves the redox ability in the SFS OCs [17]. Hence, adding metals such as Mn, Ni, and Cu in the SFS OC may positively affect the CL-SMR process. Few studies have been performed on SFS containing metals in the CL-SMR process. Furthermore, OCs containing various elements are complex.

Previous investigations have been conducted on the use of OCs in the CL-SMR process in a multi-stage reactor. Still, these reactor systems are not able to perform at all the operating conditions and the interaction effect between different parameters [20,21,29,30,31]. The RSM is a widely used mathematical and statistical method for modeling and analyzing a process in which the response of interest is affected by various variables and the objective of this method is to optimize the response [30,31].

The Box-Behnken (BBD) is one of the effective techniques to overcome this issue. Through this method, the interaction of different parameters has been designed and optimized through statistical methods [17,20,29,30,31]. The major purpose of this investigation was to synthesize the SFS OCs with different MOs. Performance evaluation of SFS OCs was investigated in a fixed bed quartz reactor for the CL-SMR process. Furthermore, RSM was used to optimize the parameters affecting the CL-SMR process under different operating conditions [20, 31].

2. Experimental method

2.1. Materials used

All materials used were obtained from Merck, Germany.

2.2. SFS oxygen carrier preparation

$Cu_xMn_{1-x}Fe_2O_4$ with (x = 0.1–0.9) SFS OCs were synthesized using a co-precipitation method. To synthesize the $Cu_xMn_{1-x}Fe_2O_4$ SFS OCs, first, $MnCl_2{\cdot}4H_2O$, $CuCl_2{\cdot}2H_2O$, and $FeCl_3$ were prepared with 1 M HCl solution mixed with the stoichiometric ratio. Next 2 M NH_3 was added dropwise to the solution to obtain pH > 8.5. The precipitate formed was washed with distilled water to remove organic impurities. Finally, the precipitate was dried for 12 h at 70 °C and calcined at 500 °C for 6 h [31,32].

2.3. SFS oxygen carrier characterization

To confirm the synthesized SFS OCs, the XRD (Philips, Xpert-MPD device) with 1.54 Å Cu Kα x-ray wavelength and 2 °C/min angular speed within 20°−80° range was used. To identify the functional groups in the SFS OCs, the FT-IR, (Bruker Tensor 27 FTIR model) within 400–4000 cm^{-1} spectral range with 4 cm^{-1} spectrum clarity was applied. The porosity and specific surface area of the SFS OCs were run through the BET, (Belsorp mini II model). The TGA analyses of the SFS OCs are run on an STA-504 thermal analyzer with a 10 °C/min (from 30 to 700 °C), heating rate, and 25 mL/min air flow. To determine the morphology and size of the particle, and identify the SFS OCs chemical compounds, the FE-SEM (QUANTA 200 model device equipped with EDX, EDAX EDS Silicon DRIFT 2017) was used.

2.4. Reactor system

The redox reactions of the synthesized SFS OCs were investigated in a fixed-bed reactor with an inner diameter of 1.2 cm and a length of 40 cm for CL-SMR. The reactor was placed inside a furnace with a height of 50 cm. The reaction temperature was controlled by a K-type thermocouple installed in the center of the furnace. To provide the steam required for the reaction. First, the distilled water was supplied to the boiler through the syringe pump and converted into vapor. Then vapor, CH_4, and N_2 with various ratios were measured by mass flow controller (MFC) with high accuracy and passed through the reactor. The reaction products go out from the reactor and cooled by a cooling system. The percentage composition of these gasses was analyzed through GC (Shimadzu 4C-TPC GC (1 m, 80/100 mesh, Rtx-Ms-5A, Rt-Q PLOT) (Fig. 1). X_{CH_4} Y_{H_2} and $S_{CO/CO2}$ were calculated using the following equations [20,23,33, 28,31,34]:

$$X_{CH_4} = \frac{(n_{CH_4})_{in} - (n_{CH_4})_{out}}{(n_{CH_4})_{in}} \times 100 \quad (1)$$

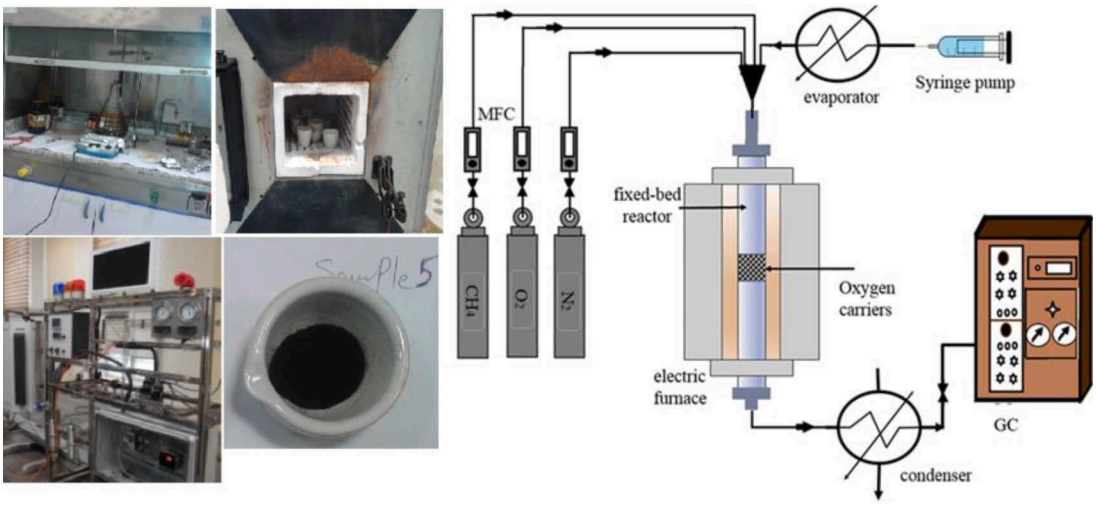

Fig. 1. Schematic showing synthesis of SFS OCs and CL-SMR reactor system [20,28,31].

$$H_2Yield = \frac{F_{H_2}}{2(F_{CH_4})_{in}} \times 100 \quad (2)$$

$$S = \frac{n_{CO}}{n_{CO_2}} \quad (3)$$

where $(n_{CH_4})_{in}$, $(n_{CH_4})_{out}$, n_{CO_2}, n_{CO}, $(F_{CH_4})_{in}$, and F_{H_2} are moles of CH_4 in, CH_4 out, CO_2, CO, CH_4 molar flow, and H_2 molar flow, respectively.

2.5. Experimental design

The RSM using BBD model was carried out to obtain the effect of the most important operational variables and optimized the responses by running the experiments. The interaction between different factors on responses and predicting the best responses was investigated using the BBD method. The most important variables of the CL-SMR process and their values in the present study are based on previous reviews and evaluations of preliminary experiments [17,20,21,35]. These process variables include reaction temperature, S/C, OC loading, X_{CH_4}, redox cycles, Y_{H_2}, and $S_{CO/CO2}$. Based on the BBD model, three levels of change are considered for each factor, including +1, 0, and −1. According to this model, twenty-nine experiments have been proposed which are shown in Table 1. The suggested SFS OCs were synthesized, and their performance was evaluated in a reactor.

3. Results and discussion

3.1. XRD of SFS OCs

The XRD patterns of the $Cu_xMn_{1-x}Fe_2O_4$ (x = 0.1- 0.9) SFS OCs are shown in Fig. 2, where the crystal planes' positions at 2θ 30.6°, 35.6°, 43.3°, 53.7°, 56.8°, and 63.3° correspond to the (220), (311), (400), (422), (511), and (440) planes, respectively [31,32]. The position and intensity of all peaks obtained from these spectra are in agreement with the standard peaks of $Mn_{0.5}Cu_{0.5}Fe_2O_4$ (JCPDS No.01–074–2072), and $MnFe_2O_4$ (JCPDS No. 380,430) [12,28,31,36–38]. The average crystallite sizes of $Cu_xMn_{1-x}Fe_2O_4$ SFS OCs are within the range of 20-70 nm and were calculated using the Debye-Scherrer equation.

3.2. FT-IR of SFS OCs

The FT-IR spectra of the $Cu_xMn_{1-x}Fe_2O_4$ (x = 0.1- 0.9) SFS OCs within the 400–3800 cm^{-1} range are shown in Fig. 3, where the peaks in the range 450–900 cm^{-1} corresponds to the MO (M-O), the hydroxyl group (O—H) corresponds to 3600–3170 cm^{-1} peaks to, the 1629 cm^{-1} peak to the H_2O group (O—H), and the very small peak at 2362 cm^{-1} corresponds to the CO_2 in the air. There exists no effect of chloride and ammonium impurity in this spectrum. The FT-IR spectra confirm the presence of pure synthesized $Cu_xNi_{0.6-x}Mn_{0.4}Fe_2O_4$ SFS OC [17,31,32,39,40].

Table 1
Testing conditions and results of the BBD model.

Run	Factors				Responses		
	Temperature (°C)	OC loading (%)	Cycle	S/C	X_{CH_4} (%)	Y_{H_2} (%)	$S_{CO/CO2}$
1	687.5	0.7	15	3.3	99.1	79.9	10.7
2	562.5	0.3	15	2.1	90.7	75.7	7.2
3	687.5	0.3	15	3.3	99.6	79.3	11.4
4	562.5	0.3	25	3.3	88	72.2	6.4
5	625	0.5	20	2.75	99.2	82.2	11.1
6	687.5	0.3	15	2.1	99.2	81.5	10.4
7	562.5	0.3	25	2.1	90	74	7.1
8	562.5	0.7	15	2.1	92	75	8.3
9	750	0.5	20	2.75	98.1	79	11.8
10	625	0.5	20	4	94.1	77	8
11	625	0.9	20	2.75	98.7	80.3	5.4
12	625	0.5	30	2.75	97.6	78.4	10.1
13	625	0.5	20	2.75	99.3	82.2	10.6
14	500	0.5	20	2.75	80.7	66.2	5
15	625	0.5	20	2.75	97.8	80	11.3
16	625	0.5	20	2.75	99.2	82.1	11.7
17	625	0.5	10	2.75	99.7	82.8	13.5
18	562.5	0.7	25	2.1	91	74.2	6.5
19	687.5	0.7	25	2.1	98.8	81.4	9.5
20	562.5	0.3	15	3.3	90	73.6	7.5
21	625	0.5	20	2.75	99.1	82.1	11.3
22	687.5	0.3	25	3.3	98.9	78.4	12.1
23	562.5	0.7	25	3.3	90.1	73.1	6.8
24	625	0.1	20	2.75	95.4	77.2	6.8
25	625	0.5	20	1.5	98	78	5.8
26	687.5	0.7	15	2.1	98.6	81.9	9.7
27	687.5	0.7	25	3.3	98.4	79	10.4
28	562.5	0.7	15	3.3	90.4	74.2	7.5
29	687.5	0.3	25	2.1	98.8	80.3	10.5

3.3. BET analysis of the SFS OCs

The BET is an important parameter in determining the OCs' performance. BET was employed to estimate gas sorption data and generate a specific surface area results expressed in units of surface area per sample mass (m^2/g). Increasing the specific surface area of the OC is an effective

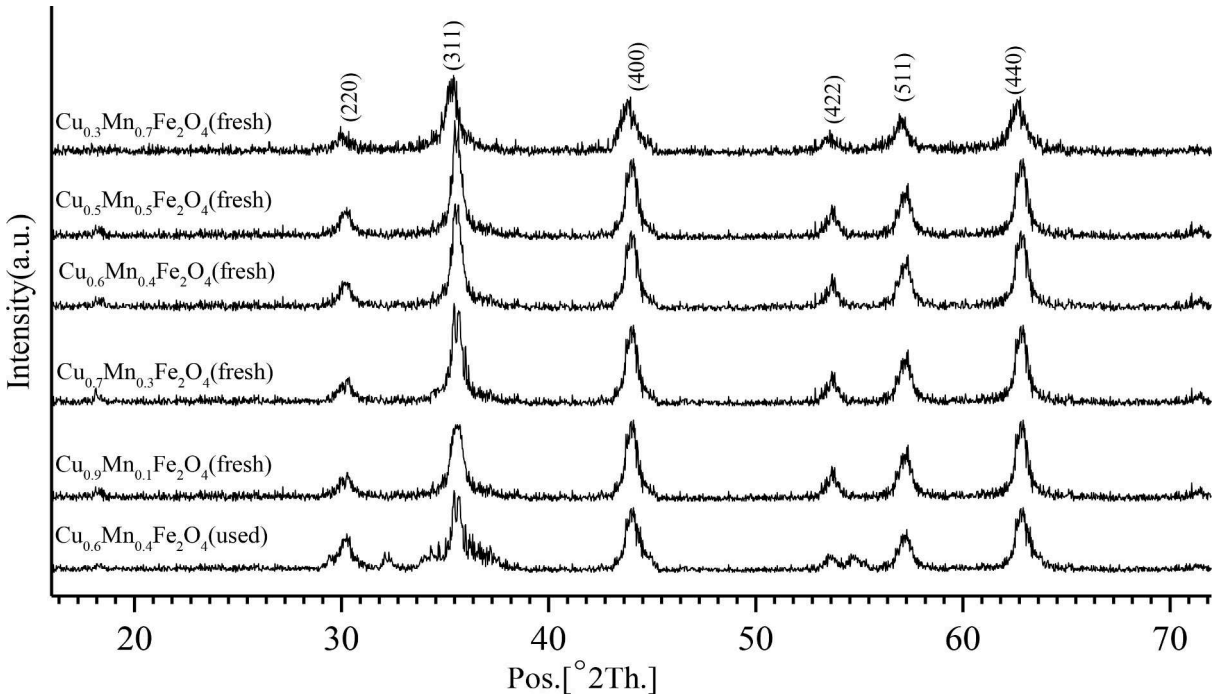

Fig. 2. XRD patterns of $Cu_xMn_{1-x}Fe_2O_4$ (x = 0.3, 0.5, 0.6, 0.7) SFS OCs and used $Cu_{0.6}Mn_{0.4}Fe_2O_4$ SFS OCs.

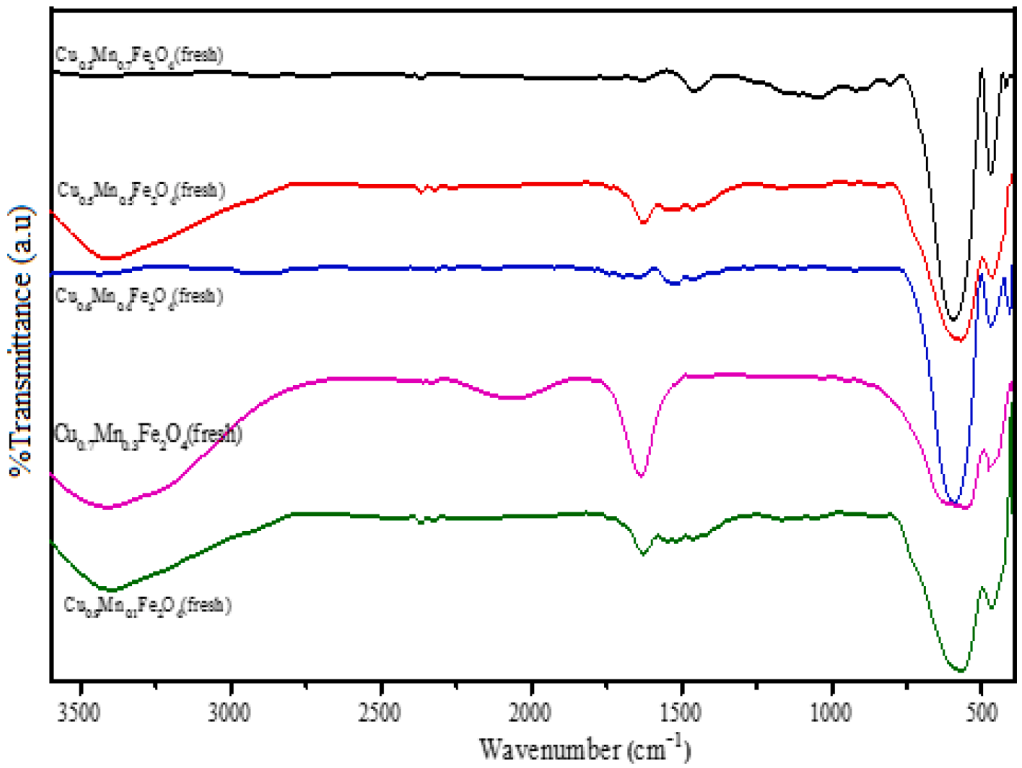

Fig. 3. FT-IR spectra of $Cu_xMn_{1-x}Fe_2O_4$ (x = 0.3, 0.5, 0.6, 0.7) SFS OCs.

parameter in the reaction of the CLC process. Therefore, with the increase of the specific surface of the OC, the mass transfer between the reactants increases [17,20,36]. The BET analysis was employed to determine the physical characteristics of the synthesized and used OCs. First, OC was heated to 250 °C to remove water vapor, CO_2, and other molecules that may occupy the pores of the OCs. Then, the samples were exposed to liquid nitrogen at a temperature of −195.79 °C, and nitrogen absorption and desorption were measured on the surface of the $Cu_xMn_{1-x}Fe_2O_4$ OCs. BET results of the synthesized and used $Cu_{0.6}Mn_{0.4}Fe_2O_4$ OCs are shown in Table 2.

3.4. Experimental design

The responses are analyzed in a statistical manner through ANOVA

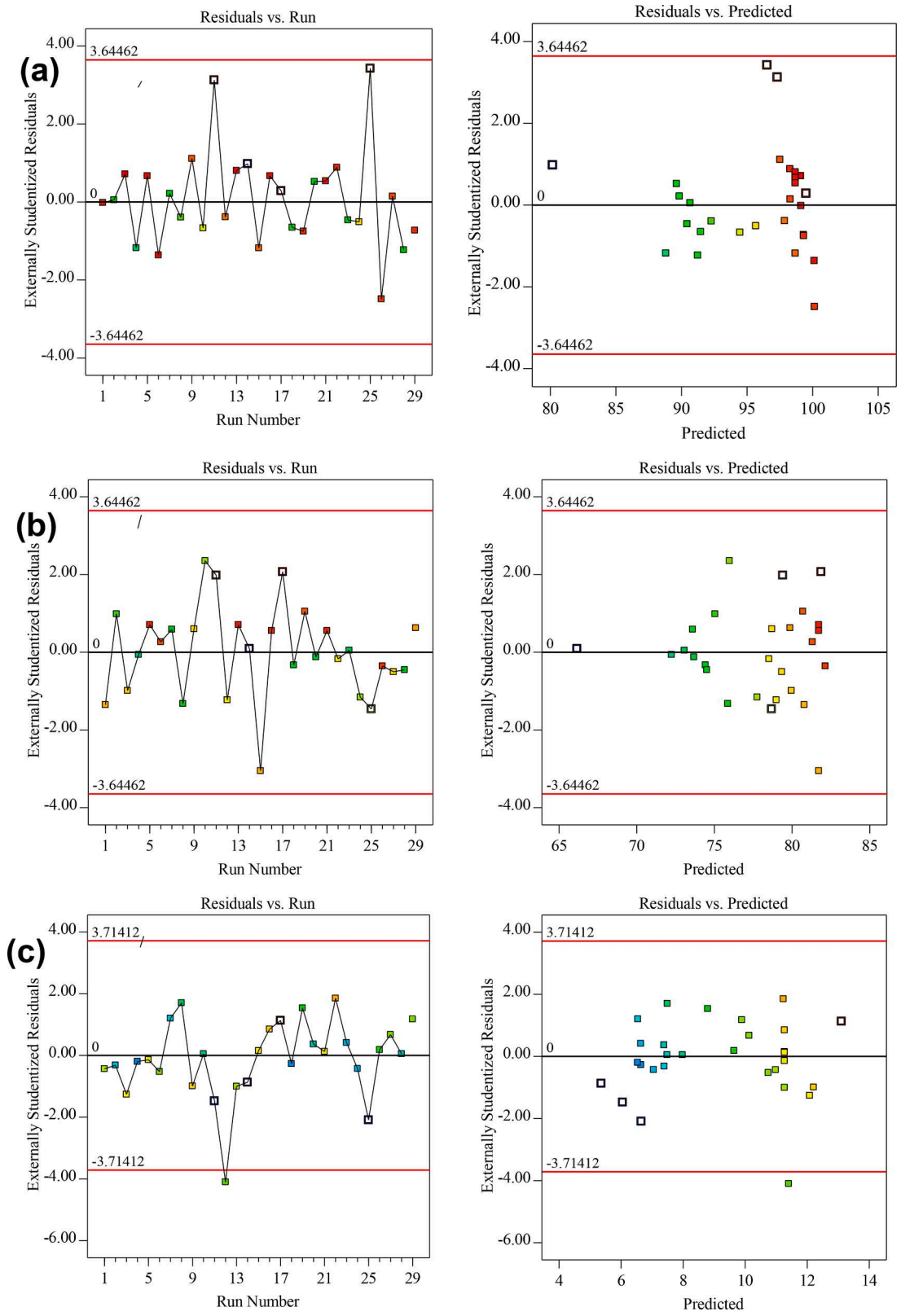

Fig. 4. The residuals versus predicted and residuals versus run for (a) X_{CH4}, (b) Y_{H_2}, and (c) S_{CO/CO_2}.

and BBD model. The data required for the statistical model for X_{CH_4}, $S_{CO/CO2}$, and Y_{H_2} are given in Table 3. The validity of the model was evaluated using F-value and P-value parameters. Low P-values and F-values lead to substantial effects on the model. P-value is a measurement to identify the significance of each parameter on the process response. That is, if the P-value is less than 0.05, the given parameter has little or no effect on the process response [9,20,21,27,41,42]. According to Table 3, P-values for X_{CH_4}, $S_{CO/CO2}$, and Y_{H_2} are 119.54, 93.06, and 36.39, respectively, which shows the significant effect of this model. R^2 for the X_{CH_4}, $S_{CO/CO2}$, and Y_{H_2} is 0.9795, 0.9738, and 0.9529, respectively. The

Table 2
BET analysis of the fresh and used SFS OCs.

Sample	Cycles	S_{BET} (m^2/g)	Vp(cm^3/g)	dp (nm)	D^b_{SEM} (nm)	D^a_{XRD} (nm)
$Cu_{0.6}Mn_{0.4}Fe_2O_4$ (fresh)	0	11.82	0.065	27.46	43	39
$Cu_{0.6}Mn_{0.4}Fe_2O_4$ (used)	30	2.93	0.027	13.14	72	77

results of R^2 indicate a good correlation between the experimental data and the proposed model. These results are in the range of 0–1, and it is closed to one, the more acceptable the prediction results of the model. The Adj R^2 for X_{CH_4}, $S_{CO/CO2}$, and Y_{H_2} is 0.9713, 0.6934, and 0.9267, respectively. The difference between R^2 and Adj R^2 for X_{CH_4}, $S_{CO/CO2}$, and Y_{H_2} is 0.0262, 0.0104, and 0.0082, respectively, which are <0.2, indicating the effectiveness of this proposed model. To enhance the validity of the quadratic model, parameters with P-value less than 0.05 are removed from the model [18,20,35]. These results are similar to [18]. The adequate precision estimates the signal-to-noise ratio, where, if this value is more than 4, it can be shown that the model is suitable. Here, this value for X_{CH_4}, $S_{CO/CO2}$, and Y_{H_2} is 43.97, 38.2774, and 19.77, respectively, indicating that this model can be employed in the design.

The normal probability plot of the residuals is a method for estimating the adequacy of the accepted models as the difference between the observed and predicted volumes [18]. The normality of the residuals means that the average difference between the residuals and the real volumes is close to 0. The closer the residual distribution to the normal distribution, the more appropriate the model fitness. The comparison of the extreme studentized residuals with X_{CH_4}, $S_{CO/CO2}$, and Y_{H_2} with real runs is illustrated in Fig. 4(a-c). Comparing the extreme studentized residuals with real runs indicates that the data distribution does not follow a specific pattern, consequently, the independence of the obtained data is acceptable. The models presented for predicting the X_{CH_4}, Y_{H_2}, and $S_{CO/CO2}$ are described as responses by using practical data via the BBD model, described by Eqs. (6-8):

The final equation for X_{CH_4}:

$$X_{CH_2} = 98.68 + 4.33A + 0.4083B - 0.4083C - 0.5167D - 0.44B - 2.64A^2 - 0.5476B^2 - 0.7976D^2 \quad (6)$$

The final equation for Y_{H2}:

$$Y_{H_2} = 81.27 + 3.14A + 0.4125B - 0.7208C - 0.6792 - 232A^2 - 0.7852B^2 - 0.3227C^2 - 1.1D^2 \quad (7)$$

The overall equation for $S_{CO/CO2}$:

$$CO/CO_2 = 11.27 + 1.17A - 0.2497B - 0.4249C + 33.23D + 0.3009AB + 0.3356AD - 0.6213A^2 - 1.18B^2 + 0.2464C^2 - 0.9885D^2 \quad (8)$$

3.5. The impact of variables and their interaction on the X_{CH_4}

The results showed that the effect of the parameters OC (x), temperature, S/C ratio, and redox cycle count on X_{CH_4} is significant. Among them, the temperature (A) parameter due to the higher F-value is the

Table 3
Evaluated regression coefficients resulted from ANOVA analysis and BBD model.

Source	X_{CH_4} (R_1)		Y_{H_2} (R_2)		$S_{CO/CO2}$ (R_3)	
	F-value	P-value	F-value	P-value	F-value	P-value
Model	119.54	< 0.0001 significant	93.06	< 0.0001 Significant	36.39	< 0.0001 significant
A-Temperature	678.34	< 0.0001	419.58	< 0.0001	173.92	< 0.0001
B- OC	6.02	< 0.0001	7.26	0.014	3.7	0.0704
C-Cycle	6.02	0.0234	22.16	0.0001	10.71	0.0042
D-S/C	9.64	0.0234	19.67	0.0003	6.55	0.0197
AB	3.58	0.0056	–	–	3.58	0.0746
AC	–	–	–	–	–	
CD	–	–	–	–	–	
AD	–	–	–	–	4.64	0.049
A^2	245.14	< 0.0001	248.76	< 0.0001	24.76	< 0.0001
B^2	12.15	0.0023	38.43	< 0.0001	89.27	< 0.0001
C^2	–	–	4.8	0.0404	3.9	0.0639
D^2	25.77	< 0.0001	55.56	< 0.0001	62.69	< 0.0001
Lack of Fit	1.84 not significant	0.2934	0.5088 not significant	0.8514	3.29 not significant	0.1295
Fit Statistics						
Std. Dev.	0.8151		0.7501		0.6359	
Mean	95.53		77.97		9.16	
C.V.%	0.8532		0.9621		6.94	
R^2	0.9795		0.9738		0.9529	
Adjusted R^2	0.9713		0.9634		0.9267	
Predicted R^2	0.9356		0.9204		0.8281	
Adeq Precision	43.97		38.2774		19.77	

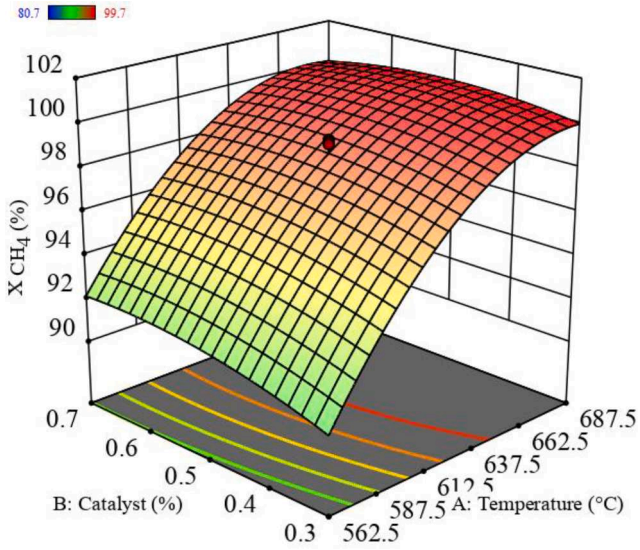

Fig. 5. The effect of variables and their interaction on the X_{CH_4} at 20th cycle and S/C = 2.75.

more significant on X_{CH_4}. As shown in Fig. 5, X_{CH_4} increased with increasing temperature. These results are consistent with the results of [20,43].

In a constant OC loading percentage (x = 0.5), by increasing the temperature (A) from 550 °C to 680 °C, the X_{CH_4} increases from 91.9 to 100. This rate has a downward trend at higher temperatures, which may be related to the accumulation of OC particles due to Cu sintering which blocks the OC pores and prevents the mass transfer between CH_4 and OC. The interaction between temperature (A) and OC loading percentage (B) on X_{CH_4} is exhibited i**n** Fig. 5. Where, as observed, in the steady conditions consisting of temperature, S/C, and cycle count (here 20), an increase in x concentration, decreases the X_{CH_4}. These results correspond to that of [26,44,45], and it can be concluded that parameter AB is one of the important characteristics of X_{CH_4}. The results from ANOVA analysis exhibit the OC loading percentage has a significant effect on the X_{CH_4}. Here, the X_{CH_4} increases in relation to that of [20,21].

3.6. The impact of variables and their interaction on Y_{H_2}

The interaction between parameters A, B, C, and D on Y_{H_2} is shown in Fig. 6. The results from ANOVA analysis exhibit that the impact of parameters A, B, C, D, A^2, B^2, C^2, and D^2 on the Y_{H_2} is significant. The temperature, OC (x), and S/C parameters has the most significant impacts on the Y_{H_2}. Whereas, the impact of cycle count on the Y_{H_2} is insignificant, meaning that the provided OC has suitable sustainability. The S/C is the most important parameter in the SMR process. By increasing the concentration of steam in this process, the Y_{H_2} increases, and the concentration of produced CO decreases. But the increase in steam concentration is not always suitable for the SMR process and leads to a decrease in efficiency and an increase in operating costs. Therefore, it is necessary to optimize the molar ratio of S/C [43,46,47]. As shown in Fig. (**6-a**), in the 20 redox cycles at 625 °C, by increasing the S/C, the Y_{H_2}, exhibits an ascending trend, followed by a downward trend. Therefore, an increase in the S/C is consistently not suitable for the SMR, hence it should be optimized. At a constant S/C, with increasing Cu (x) in $Cu_xMn_{1-x}Fe_2O_4$ SFS OC. At first, Y_{H_2} increases and then decreases slightly at high Cu loading. This phenomenon may be because of the presence of active iron oxides in the spinel structures. The sintering phenomenon caused by the melting of Cu is covered at higher temperatures and leads to the reduction of the active surface of OC and the blocking of OC pores.

As redox cycles increase, the reduction of the LO in the OC is expected and it leads to a decrease in the X_{CH_4} and Y_{H_2}. As shown in Figure (**6-b**), under a constant condition consisting of temperature, OC (x), and S/C, the Y_{H_2} does not decrease significantly with an increasing number of redox cycles. This is because the oxygen-free ferrite and its fully reduced products can improve their LO through the oxidation of CO_2 and the reduction of produced CO_2 [20,21,31,47]. The interaction between temperature and OC (x) in cycle 20th and S/C = 2.75 is shown in **Fig.** (**6-c**). The results showed that by increasing the reaction temperature, the Y_{H_2} increases at x = 0.3 and 570 °C to 670 °C from 74 to 81.15%, respectively. The collapse of the SFS OCs and the formation of the α-Fe_2O_3 phase lead to the conversion of CO and H_2 into CO_2 and H_2O [10]. It is anticipated that with an increase in the cycles' count, this phenomenon increases and generates coke on the OC surface, thus, leading to the unsuitable cracking of CH_4 and the reduction in Y_{H_2}. As illustrated in **Figures** (**5** and **6**), the X_{CH_4} and Y_{H_2} remain steady in 24 redox cycles, exhibiting no or slight spinel structure collapse has happened. These results do not correspond to that of [13,19,20,28,30,48]. After various consecutive redox cycles, no significant change in structure appeared in the OC. high X_{CH_4} average, high Y_{H_2}, High sustainability, and low created carbon on the OC surface in 24 consecutive cycles are the advantageous of this OC.

3.7. Determining the optimized conditions

The optimal X_{CH_4}, $S_{CO/CO2}$, and Y_{H_2} are selected via the suitableness of the functionality [10,20,28,48]. To achieve this optimal value, the variables consisting of temperature (550–750 °C), OC (x = 0.1–0.9), S/C (1.5–4), and 30 redox cycles' count are selected based on their level of importance (Table 4). The temperature is one of the essential and effective parameters in CH_4 cracking. As illustrated in Fig. 5, in the temperature range 600–687 °C X_{CH_4} is >99%, therefore, the level of importance of temperature 3 is assumed. In general, appropriateness is determined within the 0–1 range, that is, the higher the appropriateness, the more appropriate will be optimized conditions. After determining the restrictions to maximize the Y_{H_2} and the X_{CH_4} and to minimize the $S_{CO/CO2}$ within the independent variables' range, the RSM S/W is applied, where subject to the imposed conditions, 10 experiments were proposed (Table 5). To optimize the temperature, OC, S/C, and redox cycles' count, the values of 651.25 °C, 0.605, 2.531, and 19.156, respectively, are proposed, which the Y_{H_2}, X_{CH4}, and $S_{CO/CO2}$, 82.844, 99.97%, and 11.147, respectively obtained at 1 appropriateness. To validate the proposed model, as significant as possible, the proposed conditions were implemented using the software in the laboratory. For this purpose, reactor temperature of 650 °C, S/C = 2.5, x = 0.6, and redox cycle 19 were determined. After conducting the reactor test in laboratory conditions, Y_{H_2}, X_{CH_4}, and $S_{CO/CO2}$ are obtained as 82.14, 99.51, and 10.46, respectively. The experimental data correspond to the predicted by BBD model.

To determine the structural analysis of the optimized OC chemical compound synthesized OC, and used OC, the FE-SEM, EDX, and MAP were used. The FESEM analysis and the spectrum obtained from analyzing the synthesized OC through EDX together with the elements present in the OC investigated based on weight percentages are shown in Fig. 7(a), where it is observed that the SFS OC particles' size is in the range of 20-90 nm with a spherical shape. Each peak of the spectrum obtained through EDX corresponds to a specific atom. Larger peaks indicate a higher concentration of the element in OC. As shown Fig. 7(a), no impurities were observed in the EDX analysis. The FE-SEM, EDX, and MAP analyses of the used OC are shown in Fig. 7(b), where, it is followed that the particle size is larger than the case where the OCs are not used in the reactor and impurities are observed on the OC surface.

The XRD analysis of the $Cu_{0.6}Mn_{0.4}Fe_2O_4$ OC used after 30 consecutive cycles are shown in Fig. 2, where, as observed, the M-Fe_2O_4 is reduced to Fe-M and wustite (Fe_xO) used as active OC in the CH_4 cracking. There is no trace of the inappropriate α-Fe_2O_3 phase in this

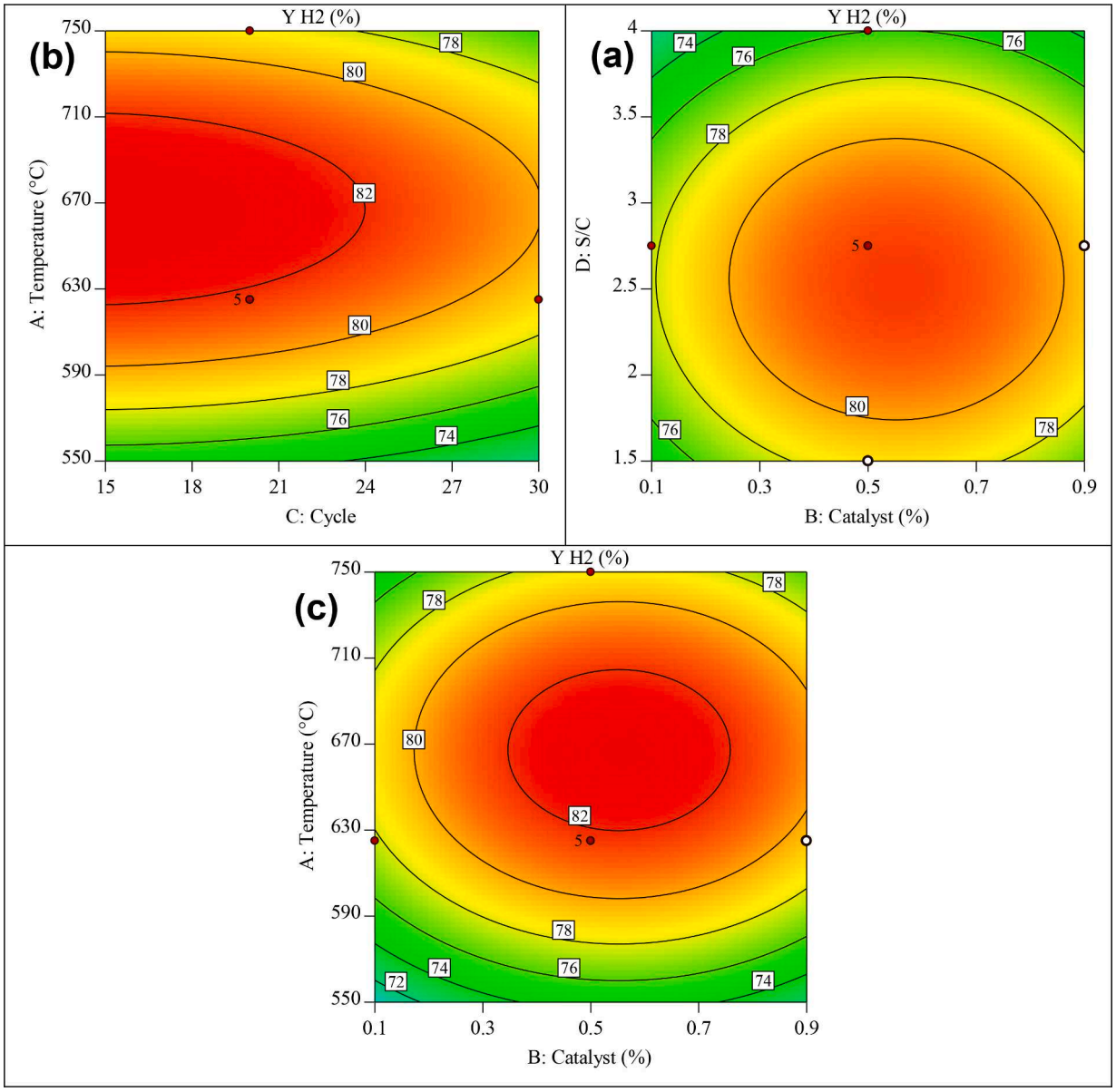

Fig. 6. The impact of variables and their interaction on the Y_{H_2} (a) Interaction between OC (x) and S/C at $T = 625$ °C and 20th cycle, (b) Interaction between temperature and redox cycles' count at $x = 0.5$ and S/C = 2.75, and (c) Interaction between temperature and OC (x) at 20th cycle and S/C = 2.75.

Table 4
The conditions imposed in determining the appropriateness functionality.

Name	Goal	Lower Limit	Upper Limit	Lower Weight	Upper Weight	Importance
A:Temperature	is in range	550	750	1	1	3
B:Catalyst	is in range	0.1	0.9	1	1	3
C:Cycle	is target = 30	15	30	1	1	5
D:S/C	is in range	1.5	4	1	1	3
$\mathbf{X_{CH4}}$	maximize	99	99.7	1	1	4
$\mathbf{Y_{H2}}$	maximize	80	82.8	1	1	5
$\mathbf{S_{CO/CO2}}$	none	5	13.6	1	1	3

Table 5
The optimized conditions obtained for Y_{H_2}, X_{CH_4}, and $S_{CO/CO2}$.

Number	Temperature	Catalyst	Cycle	S/C	X_{CH_4}	Y_{H_2}	$S_{CO/CO2}$	Desirability
1	684.623	0.498	15.611	2.607	99.01	83.078	12.702	1.000
2	670.431	0.551	15.739	2.399	99.91	83.243	11.895	1.000
3	**651.250**	**0.605**	**19.156**	**2.531**	**99.97**	**82.844**	**11.147**	**1.000**
4	691.015	0.537	17.768	2.652	99.73	82.830	12.342	1.000
5	658.529	0.629	15.647	2.574	99.63	83.161	11.584	1.000
6	686.537	0.515	16.331	2.822	99.73	82.846	12.812	1.000
7	657.467	0.640	18.295	2.470	99.34	82.920	10.879	1.000
8	656.689	0.519	18.475	2.806	99.33	82.865	12.119	1.000
9	661.211	0.573	17.050	2.497	99.67	83.212	11.699	1.000
10	665.977	0.509	17.781	2.242	99.57	82.879	11.235	1.000

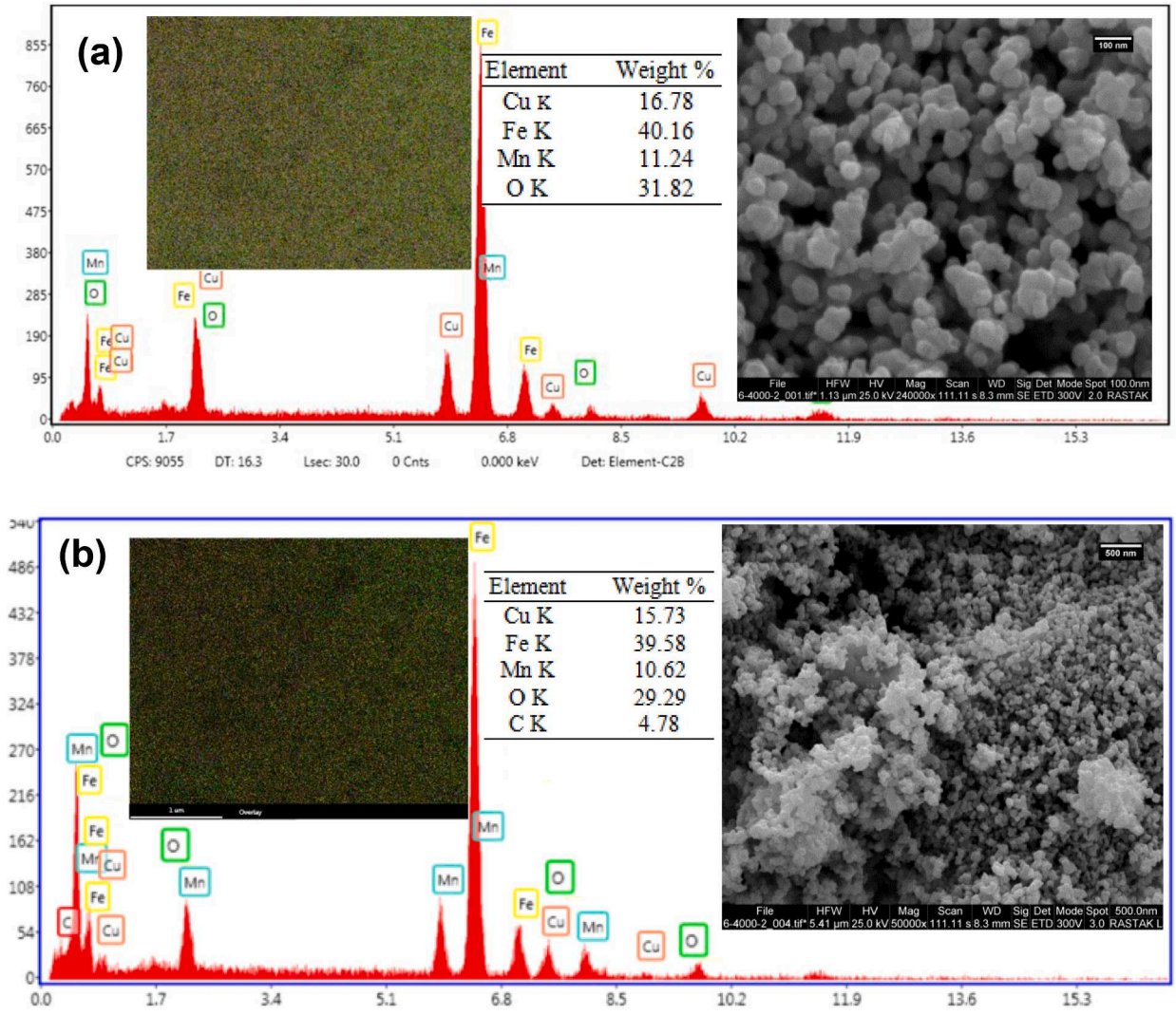

Fig. 7. FESEM, EDX, and mapping (a) synthesized $Cu_{0.6}Mn_{0.4}Fe_2O_4$ OC and (b) used $Cu_{0.6}Mn_{0.4}Fe_2O_4$ OC at 650 °C, S/C = 2.5, and 30 redox cycles.

investigation.

The most important reason for the deactivation of OC in the SMR process is the formation of carbon on the OC. There are three different types of carbon. Monoatomic carbon species (Cα) that oxidize at a temperature lower than 400 °C and cause the formation of synthesis gas. Cβ species are oxidized at 500 - 600 °C and are usually converted to amorphous carbon, but it is also possible to convert from Cα to carbon Cγ. Graphite Cγ and species are formed at temperatures higher than 650 °C and are the most stable carbon species and are the main OC deactivators [28,49–52]. Therefore, the formation and accumulation of Cβ and Cγ species can deactivate the OC. TGA analysis on SF OC $Cu_{0.6}Mn_{0.4}Fe_2O_4$ used in reaction temperature conditions of 650 °C, S/C = 2.5, and 30 cycles, is shown in Fig. 8. The initial weight loss in the temperature range of 300 °C is related to the removal of Cα carbon species. The secondary weight loss at temperatures above 500 °C is due to the oxidation of graphite carbon to carbon dioxide. It can be concluded that the formation of inactive carbon species Cβ and Cγ on the surface of the OC has caused the OC to be inactive.

As shown in Fig. 9, the X_{CH_4}, H_2/CO ratio, Y_{H_2}, and CO_2 selectivity in 30 redox cycles are stable, exhibiting no collapse in the SFS OC. Therefore, after several consecutive redox steps, no phase change has taken place in the structure of these synthesized SFS OC. The

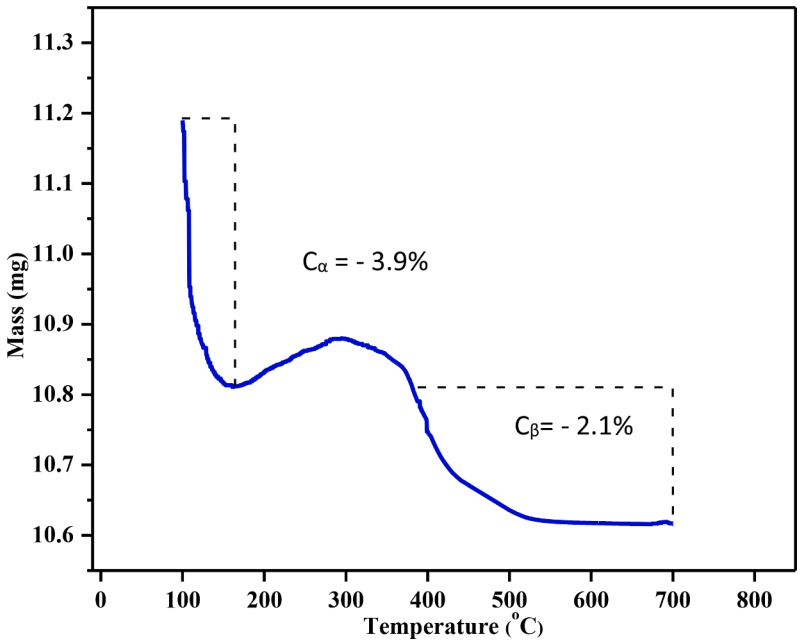

Fig. 8. TGA profile of the used catalyst obtained with a reaction temperature of 650 °C and S/C = 2.5 in 30 cycles.

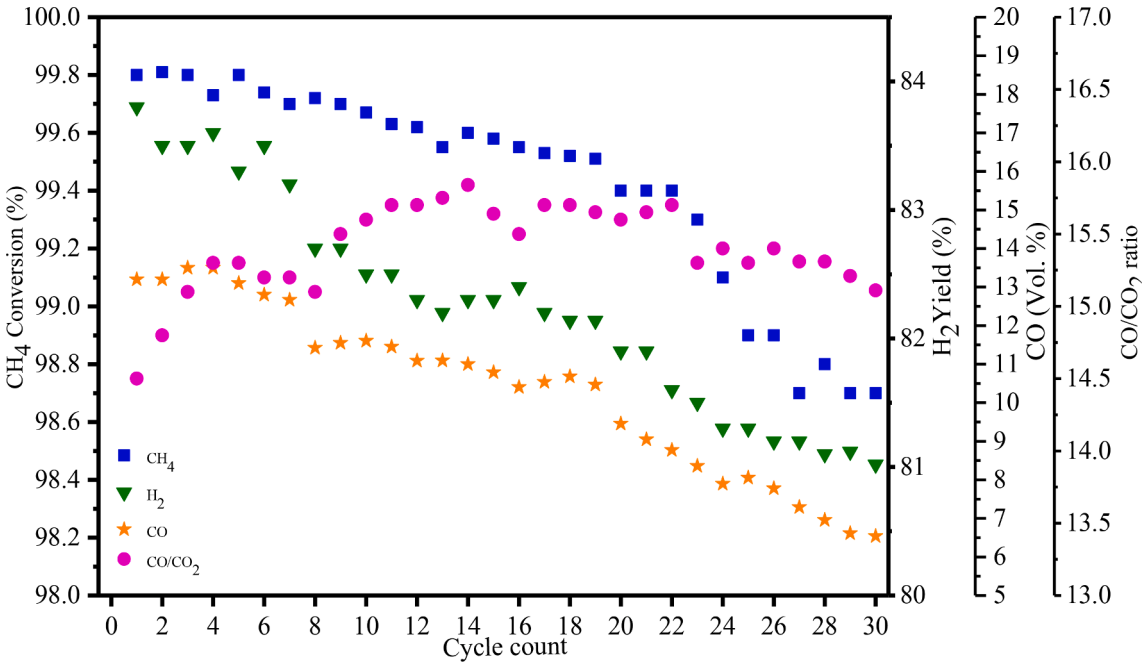

Fig. 9. The X_{CH_4}, CO_2 selectivity, Y_{H_2}, and H_2/CO for $Cu_{0.6}Mn_{0.4}Fe_2O_4$ OC in 30 redox cycles at S/C = 2.5 and 650 °C.

$Cu_{0.6}Mn_{0.4}Fe_2O_4$ SFS OC can reduce to Fe-M and wustite (Fe_xO) and control the OC sintering and the α-Fe_2O_3 phase formation. As followed in Fig. 9, the high sustainability, high X_{CH_4}, high Y_{H_2}, and rather low produced carbon on the OC surface in 30 cycles are thought the benefits of this OC with the OCs of the Cu and Mn SFS [20,21,28,53,54], Fe-based of [13,28,47], and perovskite OCs [4,9,10,13,55].

4. Conclusion

The spinel-ferrite structures (SFS) oxygen carrier (OC) $Cu_xMn_{1-x}Fe_2O_4$ with (x = 0.1 - 0.9) were successfully synthesized by the co-precipitation method. The SFS OCs were characterized using XRD, FT-IR, FESEM with X-ray spectroscopy, EDX, and BET. RSM based on the BBD model with operating variables including temperature, OC (x), and S/C and responses including X_{CH_4}, $S_{CO/CO2}$, and Y_{H_2} was applied to use $Cu_xMn_{1-x}Fe_2O_4$ with (x = 0.1–0.9) SFS OC in the CL-SMR process. The F-value for X_{CH_4}, $S_{CO/CO2}$, and Y_{H_2} are 119.54, 93.06, and 36.39, respectively, exhibiting the significant capability of this model. The impact of variables and their interaction on the X_{CH_4} indicates that the parameters A, B, C, D, AB, A^2, and D^2 are significant, and by increasing the temperature, the X_{CH_4} increases. The impacts of variables and their interaction on the Y_{H_2} indicate that the parameters A, B, C, D, A^2, B^2, C^2, and D^2 are the most effective; while an increase in the redox cycles' count has no significant effect on this yield, indicating that SFS OC has relatively appropriate sustainability. The optimized conditions are determined for maximizing the $Y_{H_2}$and X_{CH_4} and minimizing the $S_{CO/CO2}$.

Based on the available conditions, 10 experiments with 1.00 appropriateness were proposed through RSM S/W. To validate this model, the suggested conditions are implemented in the laboratory to the possible extent, where the Y_{H_2}, X_{CH_4}, and $S_{CO/CO2}$, of 81.02, 98.7, and 6.54, respectively were obtained, suggesting that this model corresponds to that of the laboratory values. The association among Cu, Mn, and Fe and the formation of the $Cu_xMn_{1-x}Fe_2O_4$ SFS exhibit high sustainability, high X_{CH_4}, high Y_{H_2}, and low produced carbon content on the OC surface in 30 redox cycles constitute the benefits of this OC. From this study, it can be deduced that the $Cu_{0.6}Mn_{0.4}Fe_2O_4$ OC can be applied as an appropriate OC in producing H_2 in the CL-SMR process.

Funding

This research did not receive any specific grant.

Research data

Data will be provided at the request.

CRediT authorship contribution statement

Mousa Nazari: Methodology, Investigation, Data curation, Writing – original draft. **Nahid Ghasemi:** Supervision, Conceptualization, Funding acquisition, Writing – review & editing. **Mohammad Mansoob Khan:** Conceptualization, Writing – review & editing. **Mahsaalsadat Rokni:** Writing – review & editing. **Seyed Reza Taghavi:** Writing – review & editing.

Declaration of Competing Interests

The authors declare that they have no known competing financial interests or personal relationships that could have appeared to influence the work reported in this paper.

Data availability

Data will be made available on request.

References

[1] T. Udomchoke, et al., Performance evaluation of sorption enhanced chemical-looping reforming for hydrogen production from biomass with modification of catalyst and sorbent regeneration, Chem. Eng. J. 303 (2016) 338–347.
[2] D.B. Bukur, L. Silvester, N. Fischer, M. Claeys, A.A. Lemonidou, On the use of an in situ magnetometer to study redox and sintering properties of NiO based oxygen carrier materials for chemical looping steam methane reforming, Int. J. Hydrogen Energy (2019).
[3] M. Rydén, P. Ramos, H 2 production with CO 2 capture by sorption enhanced chemical-looping reforming using NiO as oxygen carrier and CaO as CO2 sorbent, Fuel Process. Technol. 96 (2012) 27–36.
[4] C. Huang, et al., In situ encapsulation of iron (0) for solar thermochemical syngas production over iron-based perovskite material, Commun. Chem. 1 (1) (2018) 55.
[5] S.G. Nadgouda, M.V. Kathe, L.S. Fan, Cold gas efficiency enhancement in a chemical looping combustion system using staged H2 separation approach, Int. J. Hydrogen Energy 42 (8) (2017) 4751–4763.
[6] Y. Zhang, Z. Chao, H.A. Jakobsen, Modelling and simulation of hydrodynamics in double loop circulating fluidizedbed reactor for chemical looping combustion process, Powder Technol. 310 (2017) 35–45.
[7] M. Luo, et al., Review of hydrogen production using chemical-looping technology, Renew. Sustain. Energy Rev. 81 (2018) 3186–3214.
[8] F. He, Y. Wei, H. Li, H. Wang, Synthesis gas generation by chemical-looping reforming using Ce-based oxygen carriers modified with Fe, Cu, and Mn oxides, Energy Fuels 23 (4) (2009) 2095–2102.
[9] L. Nalbandian, A. Evdou, V. Zaspalis, La 1- x Sr x M y Fe 1- y O 3- $δ$ perovskites as oxygen-carrier materials for chemical-looping reforming, Int. J. Hydrogen Energy 36 (11) (2011) 6657–6670.
[10] Z. Yang, et al., Chemical-looping reforming of methane over La-Mn-Fe-O oxygen carriers: effect of calcination temperature, Chem. Eng. Sci. 229 (2021), 116085.
[11] Z. Yu, et al., Iron-based oxygen carriers in chemical looping conversions: a review, Carbon Resour. Convers. 2 (1) (2019) 23–34.
[12] J. Chen, K. Zhao, Z. Zhao, F. He, Z. Huang, G. Wei, Identifying the roles of MFe2O4 (M= Cu, Ba, Ni, and Co) in the chemical looping reforming of char, pyrolysis gas and tar resulting from biomass pyrolysis, Int. J. Hydrogen Energy 44 (10) (2019) 4674–4687.
[13] S. Bhavsar, N. Isenberg, A. More, G. Veser, Lanthana-doped ceria as active support for oxygen carriers in chemical looping combustion, Appl. Energy 168 (2016) 236–247.
[14] Y. Zhang, E. Doroodchi, B. Moghtaderi, Chemical looping combustion of ultra low concentration of methane with Fe2O3/Al2O3 and CuO/SiO2, Appl. Energy 113 (2014) 1916–1923.
[15] F.C. Chang, P.H. Liao, C.K. Tsai, M.C. Hsiao, H.P. Wang, Chemical-looping combustion of syngas with nano CuO–NiO on chabazite, Appl. Energy 113 (2014) 1731–1736.
[16] S.A. Wassie, F. Gallucci, A. Zaabout, S. Cloete, S. Amini, M. van Sint Annaland, Hydrogen production with integrated CO2 capture in a novel gas switching reforming reactor: proof-of-concept, Int. J. Hydrogen Energy 42 (21) (2017) 14367–14379.
[17] I. Alirezaei, A. Hafizi, M.R. Rahimpour, Syngas production in chemical looping reforming process over ZrO2 promoted Mn-based catalyst, J. CO2 Util. 23 (2018) 105–116.
[18] S. Jiang, L. Shen, J. Wu, J. Yan, T. Song, The investigations of hematite-CuO oxygen carrier in chemical looping combustion, Chem. Eng. J. 317 (2017) 132–142.
[19] K. Zhao, et al., Synergistic improvements in stability and performance of the double perovskite-type oxides La2- xSrxFeCoO6 for chemical looping steam methane reforming, Appl. Energy 197 (2017) 393–404.
[20] M. Nazari, A. Heydari Nasab, M. Soltanieh, B. Maddah, Synthesis and optimization of CuxNi0. 6-xMn0. 4Fe2O4 oxygen carrier for chemical looping steam methane reforming, Energy Sources, Part A Recover. Util. Environ. Eff. (2021) 1–19.
[21] A. Löfberg, J. Guerrero-Caballero, T. Kane, A. Rubbens, L. Jalowiecki-Duhamel, Ni/CeO2 based catalysts as oxygen vectors for the chemical looping dry reforming of methane for syngas production, Appl. Catal. B Environ. 212 (2017) 159–174.
[22] H.S. Lim, D. Kang, J.W. Lee, Phase transition of Fe2O3–NiO to NiFe2O4 in perovskite catalytic particles for enhanced methane chemical looping reforming-decomposition with CO2 conversion, Appl. Catal. B Environ. 202 (2017) 175–183.
[23] M. Gil-Calvo, C. Jimenez-Gonzalez, B. de Rivas, J.I. Gutiérrez-Ortiz, R. Lopez-Fonseca, Effect of Ni/Al molar ratio on the performance of substoichiometric NiAl2O4 spinel-based catalysts for partial oxidation of methane, Appl. Catal. B Environ. 209 (2017) 128–138.
[24] M. Abbasi, M. Farniei, M.R. Rahimpour, A. Shariati, Hydrogen production in an environmental-friendly process by application of chemical looping combustion via Ni- and Fe-Based oxygen carriers, Theoretic. Found. Chem. Eng. 49 (6) (2015) 884–900.
[25] M. Ismail, W. Liu, M.T. Dunstan, S.A. Scott, Development and performance of iron based oxygen carriers containing calcium ferrites for chemical looping combustion and production of hydrogen, Int. J. Hydrogen Energy 41 (7) (2016) 4073–4084.
[26] D.D. Miller, R. Siriwardane, J. Poston, Fluidized-bed and fixed-bed reactor testing of methane chemical looping combustion with MgO-promoted hematite, Appl. Energy 146 (2015) 111–121.
[27] P.-.C. Kuo, J.-.R. Chen, W. Wu, J.-.S. Chang, Hydrogen production from biomass using iron-based chemical looping technology: validation, optimization, and efficiency, Chem. Eng. J. 337 (2018) 405–415.
[28] M. Nazari, M. Soltanieh, A. Heydarinasab, B. Maddah, Synthesis of a new self-supported Mgy (CuxNi0. 6-xMn0. 4) 1-yFe2O4 oxygen carrier for chemical looping steam methane reforming process, Int. J. Hydrogen Energy (2021).
[29] Z. Huang, et al., Evaluation of multi-cycle performance of chemical looping dry reforming using CO2 as an oxidant with Fe–Ni bimetallic oxides, J. energy Chem. 25 (1) (2016) 62–70.
[30] H.R. Forutan, E. Karimi, A. Hafizi, M.R. Rahimpour, P. Keshavarz, Expert representation chemical looping reforming: a comparative study of Fe, Mn, Co and Cu as oxygen carriers supported on Al2O3, J. Ind. Eng. Chem. 21 (2015) 900–911.
[31] M. Nazari, A. Heydarinasab, M. Soltanieh, B. Maddah, Synthesis and optimization of NixMn1-xFe_2O_4 catalyst in chemical looping steam methane reforming process, Iran. J. Chem. Chem. Eng. Res. Artic. 40 (5) (2021).
[32] M. Nazari, N. Ghasemi, H. Maddah, M.M. Motlagh, Synthesis and characterization of maghemite nanopowders by chemical precipitation method, J. Nanostructure Chem. 4 (2) (2014) 99.
[33] A. Evdou, V. Zaspalis, L. Nalbandian, Ferrites as redox catalysts for chemical looping processes, Fuel 165 (2016) 367–378.
[34] S. Ma, S. Chen, A. Soomro, W. Xiang, Effects of supports on hydrogen production and carbon deposition of Fe-based oxygen carriers in chemical looping hydrogen generation, Int. J. Hydrogen Energy 42 (16) (2017) 11006–11016.
[35] Y. De Vos, M. Jacobs, P. Van Der Voort, I. Van Driessche, F. Snijkers, A. Verberckmoes, Sustainable iron-based oxygen carriers for chemical looping for hydrogen generation, Int. J. Hydrogen Energy 44 (3) (2019) 1374–1391.
[36] S.G. Nadgouda, M. Guo, A. Tong, L.-.S. Fan, High purity syngas and hydrogen coproduction using copper-iron oxygen carriers in chemical looping reforming process, Appl. Energy 235 (2019) 1415–1426.
[37] F. Liu, J. Liu, Y. Yang, Z. Wang, C. Zheng, Reaction mechanism of spinel CuFe2O4 with CO during chemical-looping combustion: an experimental and theoretical study, Proc. Combust. Inst. 37 (4) (2019) 4399–4408.
[38] R. Pérez-Vega, A. Abad, M.T. Izquierdo, P. Gayán, L.F. de Diego, J. Adánez, Evaluation of Mn-Fe mixed oxide doped with TiO2 for the combustion with CO2 capture by chemical looping assisted by oxygen uncoupling, Appl. Energy 237 (2019) 822–835.

[39] M. Ortiz, et al., Hydrogen production with CO2 capture by coupling steam reforming of methane and chemical-looping combustion: use of an iron-based waste product as oxygen carrier burning a PSA tail gas, J Power Sources 196 (9) (2011) 4370–4381.
[40] P. Hallberg, M. Hanning, M. Rydén, T. Mattisson, A. Lyngfelt, Investigation of a calcium manganite as oxygen carrier during 99h of operation of chemical-looping combustion in a 10 kWth reactor unit, Int. J. Greenh. gas Control 53 (2016) 222–229.
[41] Y. Patcharavorachot, N. Chatrattanawet, A. Arpornwichanop, S. Assabumrungrat, Optimization of hydrogen production from three reforming approaches of glycerol via using supercritical water with in situ CO2 separation, Int. J. Hydrogen Energy 44 (4) (2019) 2128–2140.
[42] A.A. Fard, R. Arvaneh, S.M. Alavi, A. Bazyari, A. Valaei, Propane steam reforming over promoted Ni–Ce/MgAl2O4 catalysts: effects of Ce promoter on the catalyst performance using developed CCD model, Int. J. Hydrogen Energy 44 (39) (2019) 21607–21622.
[43] K. Maaz, et al., Fabrication and size dependent magnetic studies of NixMn1-xFe2O4 (x= 0.2) cubic nanoplates, J. Alloys Compd. 684 (2016) 656–662.
[44] M.M. Hossain, H.I. de Lasa, Chemical-looping combustion (CLC) for inherent CO2 separations—a review, Chem. Eng. Sci. 63 (18) (2008) 4433–4451.
[45] Y. Zhang, E. Doroodchi, B. Moghtaderi, Chemical looping combustion of ultra low concentration of methane with Fe2O3/Al2O3 and CuO/SiO2, Appl. Energy 113 (2014) 1916–1923.
[46] A. Hafizi, M.R. Rahimpour, S. Hassanajili, Hydrogen production by chemical looping steam reforming of methane over Mg promoted iron oxygen carrier: optimization using design of experiments, J. Taiwan Inst. Chem. Eng. 62 (2016) 140–149.
[47] Y. Sun, Y. Diao, H. Wang, G. Chen, M. Zhang, M. Guo, Synthesis, structure and magnetic properties of spinel ferrite (Ni, Cu, Co) Fe2O4 from low nickel matte, Ceram. Int. 43 (18) (2017) 16474–16481.
[48] S.M. Ramay, S.A. Siddiqi, S. Atiq, M. Saleem, A. Mahmood, S. Naseem, Low-temperature synthesis by autocombustion and investigation of structural and magnetic properties of Mn 0.5 Cu 0.5- x Ni x Fe 2 O 4 nanocrystallites, IEEE Trans. Magn. 50 (8) (2014) 1–4.
[49] Y. Zhang, W. Wang, Z. Wang, X. Zhou, Z. Wang, C.-.J. Liu, Steam reforming of methane over Ni/SiO2 catalyst with enhanced coke resistance at low steam to methane ratio, Catal. Today 256 (2015) 130–136.
[50] D. Cheng, X. Zhu, Y. Ben, F. He, L. Cui, C. Liu, Carbon dioxide reforming of methane over Ni/Al2O3 treated with glow discharge plasma, Catal. Today 115 (1–4) (2006) 205–210.
[51] X. Zhai, S. Ding, Z. Liu, Y. Jin, Y. Cheng, Catalytic performance of Ni catalysts for steam reforming of methane at high space velocity, Int. J. Hydrogen Energy 36 (1) (2011) 482–489.
[52] K. Urasaki, Y. Sekine, S. Kawabe, E. Kikuchi, M. Matsukata, Catalytic activities and coking resistance of Ni/perovskites in steam reforming of methane, Appl. Catal. A Gen. 286 (1) (2005) 23–29.
[53] M. Khaleghi, H. Moradmard, S.F. Shayesteh, Cation distributions and magnetic properties of Cu-doped nanosized MnFe 2 O 4 synthesized by the coprecipitation method, IEEE Trans. Magn. 54 (1) (2017) 1–5.
[54] R. Noroozi, M. Gholami, M. Farzadkia, A.Jonidi Jafari, Degradation of ciprofloxacin by CuFe2O4/GO activated PMS process in aqueous solution: performance, mechanism and degradation pathway, Int. J. Environ. Anal. Chem. (2020) 1–22.
[55] L. Protasova, F. Snijkers, Recent developments in oxygen carrier materials for hydrogen production via chemical looping processes, Fuel 181 (2016) 75–93.